Supplementary Information (SI) for Energy & Environmental Science.

Interatomic Fe-Cu Cooperation in Nitrogen-Doped Carbon for Enhanced Oxygen Reduction

Xiang Ao, Linfeng Li, Yong Ding, Gyutae Nam, Bote Zhao,* Chundong Wang* and Meilin Liu*

Table of Contents

1. Experimental and Computational Details

Chemicals

Zinc nitrate hexahydrate, 2-methylimidazole, iron nitrate nonahydrate, iron(II) phthalocyanine (FePc), copper(II) phthalocyanine (CuPc), methanol, ethanol, hexane and potassium hydroxide were purchased from Sigma Aldrich. Copper nitrate hemi(pentahydrate), commercial Pt/C (20 wt.%, HiSPEC3000) and Nafion dispersion (5 wt.%) were purchased from Alfa Aesar. All the chemicals were used without any further purification. The ultrapure water (18.2 MΩ·cm) used in all experiments was obtained through ion exchange and filtration.

Preparation of ZIF-8

$Zn(NO)_3•6H_2O$ (4.464 g) was dissolved in 120 mL of methanol with stirring, then 2-methylimidazole (4.928 g) in 120 mL of methanol was subsequently poured into above solution followed by vigorous stirring for 6 h at room temperature. The as-obtained product was centrifuged and washed with methanol several times and finally dried overnight in oven.

Preparation of NC

NC was synthesized by calcining the ZIF-8 directly. Typically, the ZIF-8 powder was placed in a tube furnace and annealed at 900 ^oC for 2 h with a heating rate of 5 ^oC min^{-1} under flowing N_2 gas and then naturally cooled to room temperature.

Preparation of Fe-NC

ZIF-8 (100 mg) was dispersed in 16 mL of hexane by sonication. Then, 60 μL of $Fe(NO_3)_3·9H_2O$ (30 mg mL^{-1}) was added dropwise to the above solution under ultrasound for more than 10 min to get a homogeneous suspension. The suspension was stirred for another 2 h at room temperature. The impregnated ZIF-8 sample was then centrifuged and dried in oven at 60 ^oC for overnight. Finally, the dried powder was placed in a tube furnace and annealed at 900 ^oC for 2 h with a heating rate of 5 ^oC min^{-1} under flowing N_2 gas and then naturally cooled to room temperature.

Preparation of Cu-NC

The synthesis procedure of Cu-NC was similar to that of the aforementioned Fe-NC, except for adding 60 μL of $Cu(NO_3)_2·2.5H_2O$ (17 mg mL^{-1}) into the ZIF-8 suspension instead of 60 μL of $Fe(NO_3)_3·9H_2O$ (30 mg mL^{-1}).

Preparation of FeCu-N-C

The synthesis procedure of FeCu-NC was similar to that of the aforementioned Fe-NC except that the metal salt solution added in to ZIF-8 suspension was changed to a solution contain both $Fe(NO_3)_3·9H_2O$ (30 mg mL^{-1}) and $Cu(NO_3)_2·2.5H_2O$ (17 mg mL^{-1}).

Preparation of Fe_2-NC

The synthesis procedure of Fe_2-NC was similar to that of the aforementioned Fe-NC except that the concentration of $Fe(NO_3)_3·9H_2O$ doubled to 60 mg mL^{-1}.

Preparation of Cu_2-NC

The synthesis procedure of Fe_2-NC was similar to that of the aforementioned Cu-NC except that the concentration of $Cu(NO_3)_2 \cdot 2.5H_2O$ doubled to 34 mg mL^{-1}.

Physical characterization

Scanning electron microscopy (SEM) analysis was performed on a Zeiss Ultra 60 FE-SEM microscopy. An aberration-corrected scanning transmission electron microscope (AC-STEM, Hitachi HD 2700) with an energy dispersive X-ray spectrometer (EDX) was employed to analyze the detailed morphology and structure information. Powder X-ray diffraction (XRD) patterns of samples were recorded using an X'Pert PRO Alpha-1 X-ray diffractometer with a Cu Kα radiation source. Raman spectroscopic measurement was performed using a Renishaw RM1000 microspectroscopic system with an Ar laser excitation (514 nm). The nitrogen adsorption-desorption isotherm of the sample was measured using a Micromeritics ASAP 2020 analyzer. X-ray photoelectron spectroscopy (XPS) measurements were recorded with a Physical Electronics PHI 5802, and all the reported binding energy data were calibrated using C 1s (284.8 eV). The metal content was confirmed by inductively coupled plasma optical emission spectrometer (ICP-OES, Varian 710ES). The X-ray absorption spectroscopy (XAS) analysis was performed on the BL10C beamline at the Pohang light source (PLS) with top-up mode operation under a ring current of 300 mA at 3.0 GeV. The acquired data were normalized to the incoming incident photon flux and processed according to the standard procedure using the ATHENA module implemented in the IFEFFIT software packages. To obtain quantitative structural parameters around central atoms, least-squares curve parameter fitting was performed using the ARTEMIS module of IFEFFIT software packages.

Electrochemical measurements

Electrochemical measurements were carried out using an electrochemical workstation (CHI 760) with a standard three-electrode cell and a rotating disk electrode (RDE) system (Pine Instrument Company, USA). The RDE with a glassy carbon disk of 5 mm in diameter was used as the substrate for the working electrode. To prepare the working electrode, 5 mg of catalyst was ultrasonically dispersed in a 1.0 mL mixture of ethanol (480 μL), water (480 μL) and Nafion (5 wt.%, 40 μL) solution to form an ink. Then 20 uL of the ink was drop-casted on the disk electrode and dried at room temperature using a rotational drying method to obtain a film electrode with a catalyst mass loading of 0.5 mg cm^{-2} for all samples including commercial Pt/C. A Ag/AgCl electrode (saturated KCl solution) and a graphite rod were used as reference and counter electrode, respectively. A 0.1 M KOH or 0.1 M $HClO_4$ aqueous solution was used as the electrolyte. The electrolyte was purged with required gas (N_2 or O_2) for at least 30 min before the test and the gas flow was maintained during the test. Cyclic voltammetry (CV) test was carried out in a N_2 or O_2-saturated electrolyte at a scan rate of 50 mV s^{-1}. The ORR activity was evaluated by linear sweep voltammetry (LSV) in O_2-saturated electrolyte collected by scanning cathodically at a scan rate of 10 mV s^{-1}, and all currents were corrected by deducting the background current that measured in a N_2-saturated electrolyte.

Rotating ring-disk electrode (RRDE) measurements were also carried out to determine the four-electron selectivity. The mass loading and diameter of the disk is the same with that of RDE. The disk electrode was scanned at a rate of 10 mV s^{-1} and a rotation rate of 1600 rpm, and the ring electrode potential was set to 1.5 V. The currents were corrected by deducting the background current that measured in N_2-saturated electrolyte. All of the potentials for RDE and RRDE tests reported in this work were calibrated to the reversible hydrogen electrode and corrected for ohmic loss.

The peroxide yield (H_2O_2 %) and the electron transfer number (n) were calculated by the following equations:

$$H_2O_2(\%) = 200 \times \frac{I_R/N}{(I_R/N) + I_D}$$

$$n = 4 \times \frac{I_D}{(I_R/N) + I_D}$$

where I_D is the disk current, I_R is the ring current and N is the ring collection efficiency, equal to 25.6 %.

Zinc-air battery

Zinc-air battery tests were performed using a home-made battery. The catalyst ink was the same as that used for RDE tests. Then the catalyst was drop-casted onto carbon fiber paper with a catalyst loading of 1 mg cm^{-2} as the air cathode. For comparison, a counterpart air cathode with the sample catalyst loading was also made using Pt/C as the catalyst. The polished Zn foil was used as the anode and the 6.0 M KOH solution was used as the electrolyte. The discharge polarization curves were recorded in ambient on an electrochemical workstation, and the galvanostatic discharge tests were carried out using a NEWARE instrument.

PEMFC electrochemical performance test

The PEMFC electrochemical performance was tested at a fuel cell test system. The MEAs with an active area of 4 cm^2 were prepared using the spray deposition method.[1,2] Nafion 211 proton exchange membranes were purchased from Fuel Cell Store and treated with 5 wt. % H2O2 and 0.5 M H_2SO_4 solutions in the water bath at 80 °C for 1 h for each step, and then washed with deionized water before use. The catalyst ink was prepared by ultrasonically mixing the catalyst powder (16 mg), isopropanol (4 mL) and 10 wt. % Nafion ionomer solution (160 mg) for 1 h. Then the ink was sprayed onto the one side of a pretreated Nafion 211 membrane at a hot plate (130 °C) to form the cathode catalyst layer. The mass loadings of the as-prepared noble-metal-free catalyst or commercial Pt/C at cathode are 4 mg cm^{-2} and 0.5 mg cm^{-2}, respectively. A commercial Pt/C catalyst was deposited at the anode side by the similar method to achieve a Pt loading of 0.2 mg cm^{-2} at the anode. The GDL (Sigracet 22 BB) was purchased from Fuel Cell Stores and used without further treatment. For H_2-O_2 fuel cell test, humidified hydrogen (200 mL min^{-1}) and oxygen (400 mL min^{-1}) were fed to the anode and cathode, respectively. The temperature of the cell was maintained at 65 °C and the backpressure of both the anode and cathode was 1 bar.

Theoretical Calculations

All spin-polarized density functional theory (DFT) calculations are performed using generalized gradient approximation (GGA) in the form of Perdew-Burke- Ernzerhof funtional (PBE) for the exchange-correlation potentials and the projector augmented wave (PAW) method[3-5]. The plane-wave basis was set of 500 eV, as implemented in the Vienna ab Initio simulation package (VASP) with consideration of spinpolarization[6-8]. The Brillouin-zone was sampled with 4×4×1 and 6×6×1 K-point grids for the structure optimizations and electron property calculations, respectively. The periodical monolayer slabs based on graphene (001) 3×3 units were separated by a vacuum zone of 15 Å. All the structures are fully optimized to a convergence threshold of 10-5 eV for energy and 0.01 eVÅ-1 for force. Visualization of the atomic structures are made by using VESTA[9].

The formation energy Ef of models was calculated according to Eq (1).

$$E_f = E_{(slab+atom)} - E_{slab} - E_{Fe(per\ atom)} - E_{Cu(per\ atom)} \quad (1)$$

where E(slab+atom) stands for the total energy of fully relaxed model we built. Eslab is the total energy of fully relaxed carbon-nitrogen slab model without Fe or Cu atom. $E_{Fe(per\ atom)}$ and $E_{Cu(per\ atom)}$ are the energy of an isolated Fe and Cu atom in its bulk phase, respectively.

The overpotentials were evaluated using a previously described approach[10]. The four-electron ORR mechanism in alkaline medium can be summarized as follows:

$$*O_2 + H_2O + e^- \rightarrow *OOH + OH^- \ (2)$$

$$*OOH + e^- \rightarrow *O + OH^- \ (3)$$

$$*O + H_2O + e^- \rightarrow *OH + OH^- \ (4)$$

$$*OH + e^- \rightarrow * + OH^- \ (5)$$

where * represents the preferable adsorption site for intermediates. For each step, the reaction free energy is calculated by

$$\Delta G = \Delta E + \Delta ZPE - T\Delta S + \Delta G_U + \Delta G_{PH} \quad (6)$$

Where ΔE is the total energy difference between reactants and products of reactions, ΔZPE and ΔS is the zero-point energy correction and entropy differences, respectively, Tis the system temperature of 298.15 K, $\Delta G_U = -eU$, where e is the elementary charge, U is the electrode potential, ΔG_{PH} is the correction of the H^+ free energy[11].

The overpotential η can be evaluated from the Gibbs free energy differences of each step as

$$\eta = 1.23\text{-min } [\Delta G_1, \Delta G_2, \Delta G_3, \Delta G_4]/e\ ] \quad (7)$$

where ΔG_1, ΔG_2, ΔG_3, and ΔG_4 are the free energy of reactions (2) to (5).

2. Supporting Figures

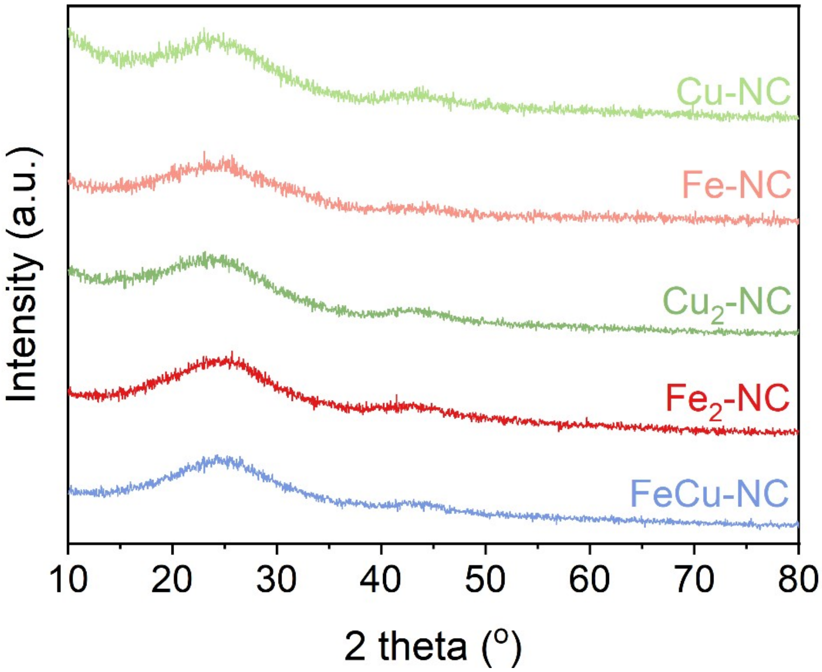

Figure S1. XRD patterns of FeCu-NC, Fe-NC, Cu-NC, Fe$_2$-NC and Cu$_2$-NC.

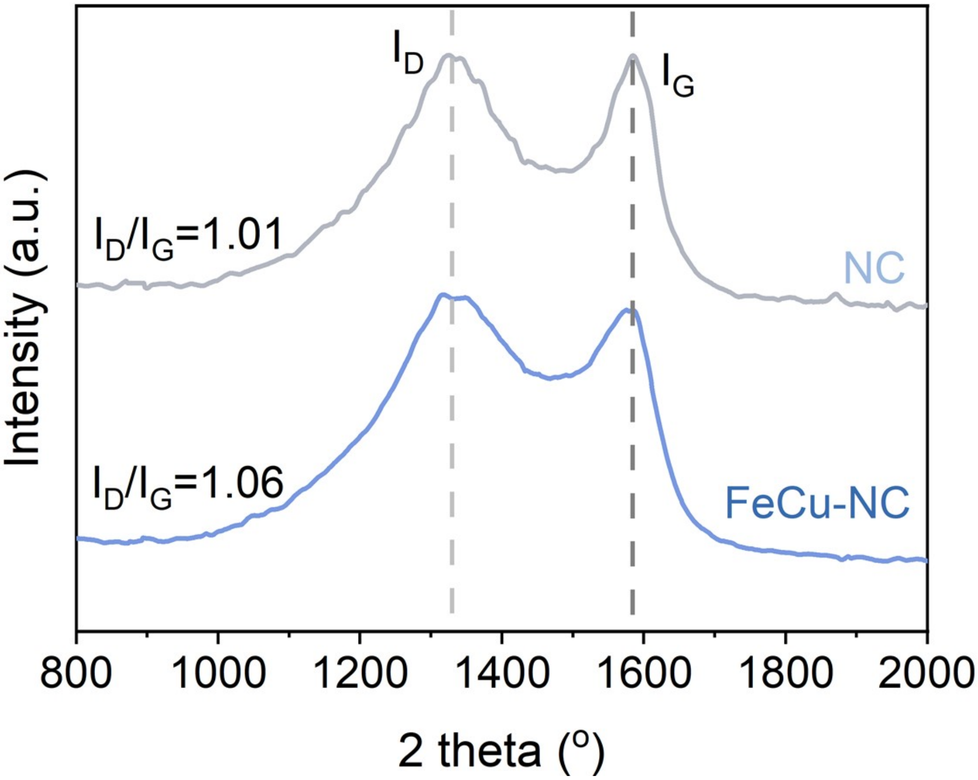

Figure S2. Raman spectra of FeCu-NC and NC.

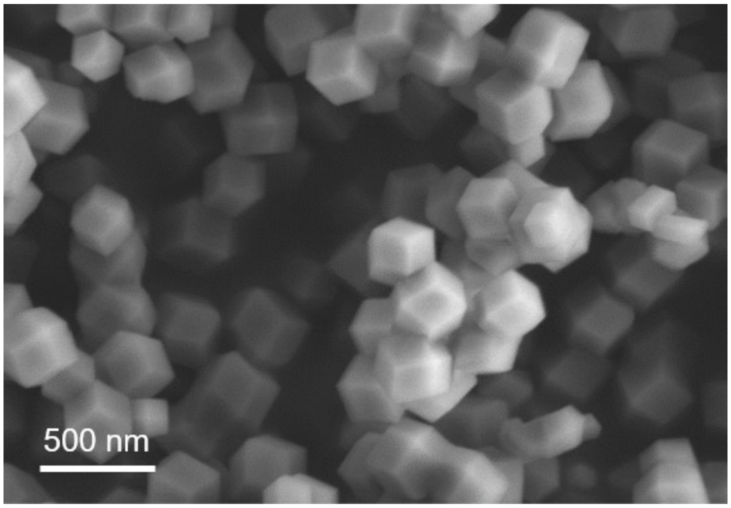

Figure S3. SEM image of ZIF-8.

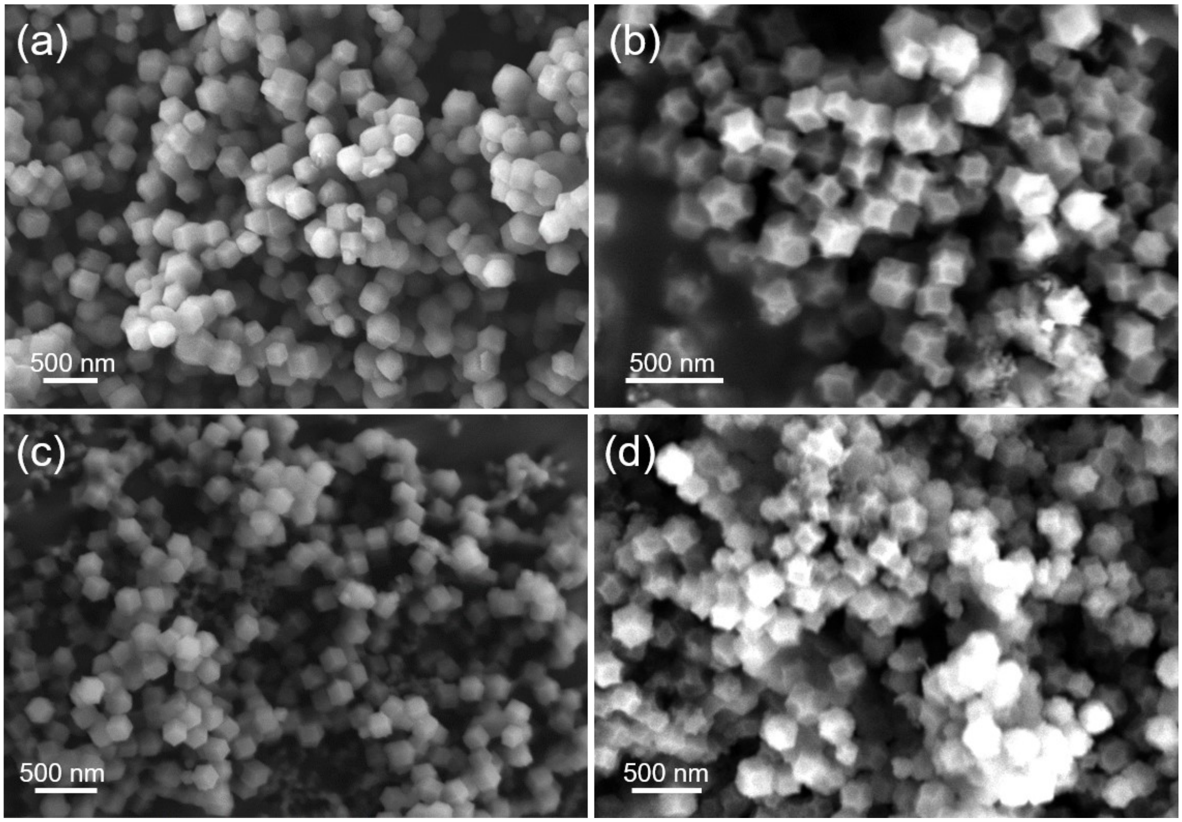

Figure S4. SEM images of (a) Cu-NC, (b)Fe-NC, (c) Cu_2-NC and (d) Fe_2-NC.

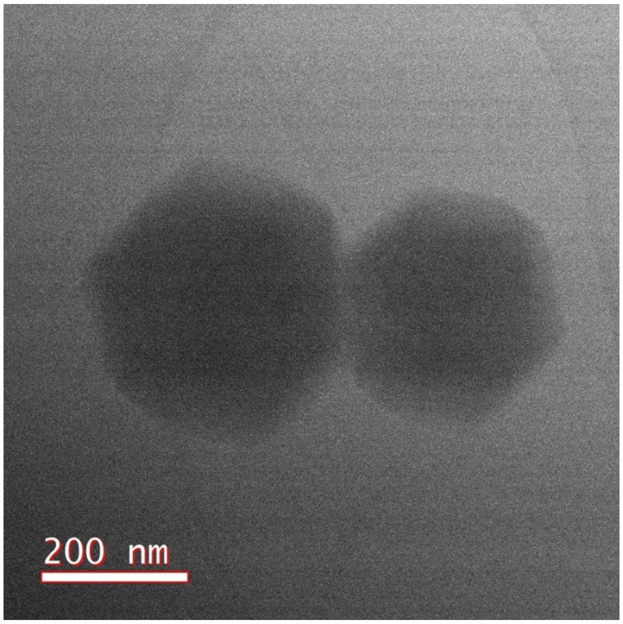

Figure S5. TEM image of FeCu-NC.

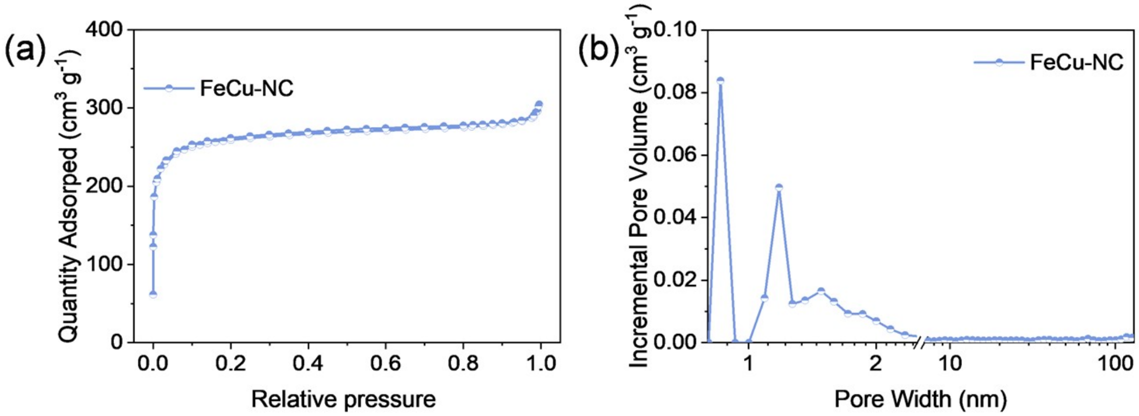

Figure S6. (a) Nitrogen adsorption-desorption isotherms for FeCu-NC and (b) the corresponding pore size distribution.

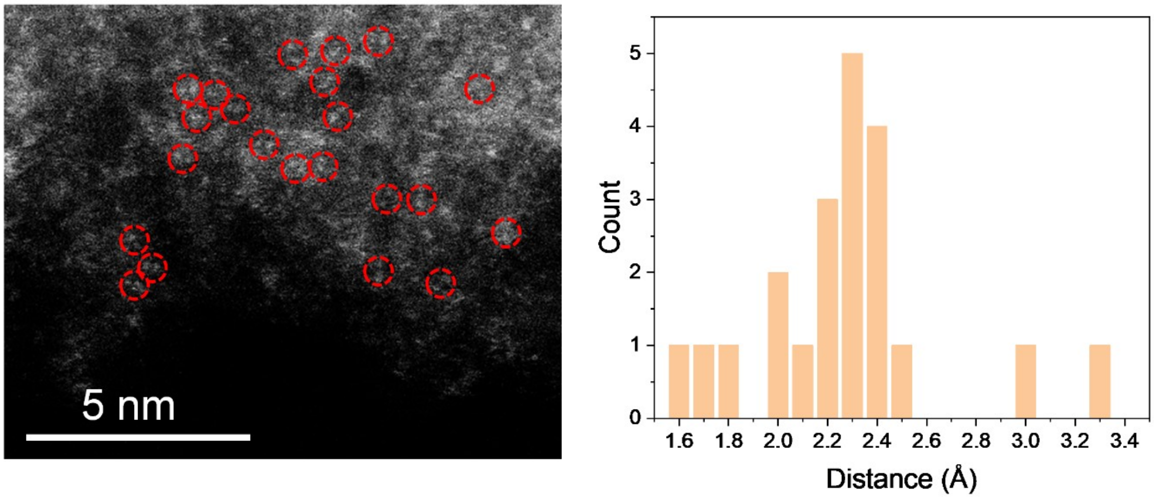

Figure S7. Aberration-corrected HAADF-STEM images of FeCu-NC and the corresponding statistical distribution of interatomic distances for dual-metal sites indicated by the red circles.

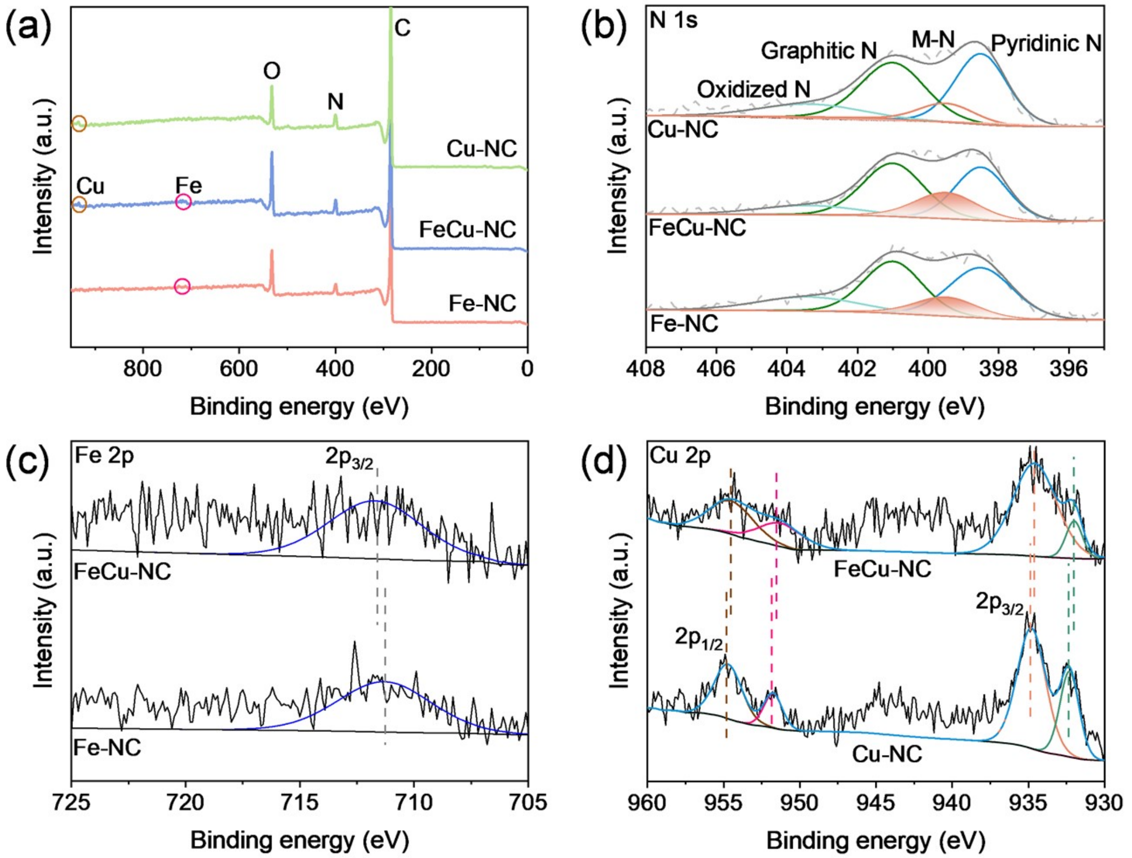

Figure S8. (a) XPS survey spectra of Cu-NC, FeCu-NC and Fe-NC. (b) N 1s spectra of Cu-NC, FeCu-NC and Fe-NC. (c) Fe 2p spectra of FeCu-NC and Fe-NC. (d) Cu 2p spectra of FeCu-NC and Cu-NC.

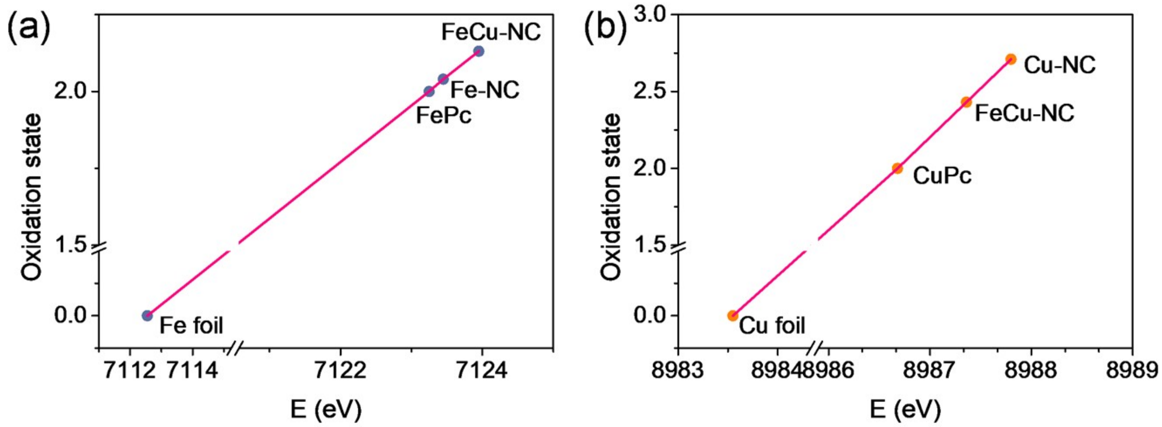

Figure S9. The fitted average oxidation state of (a) Fe and (b) Cu in the samples from the the absorption edge of Fe and Cu K-edge.

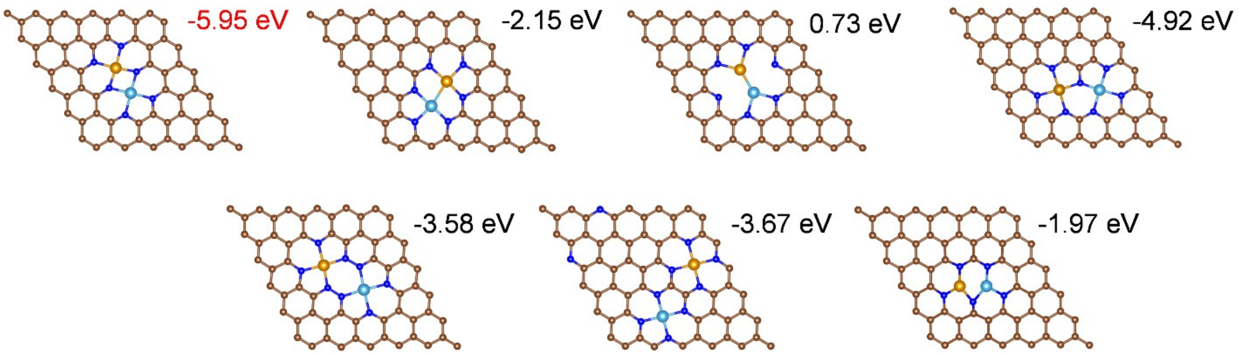

Figure S10. Calculated formation energies for various dual-metal configurations. The gray, cyan, orange, and blue spheres represented the C, N, Fe, and Cu atoms, respectively.

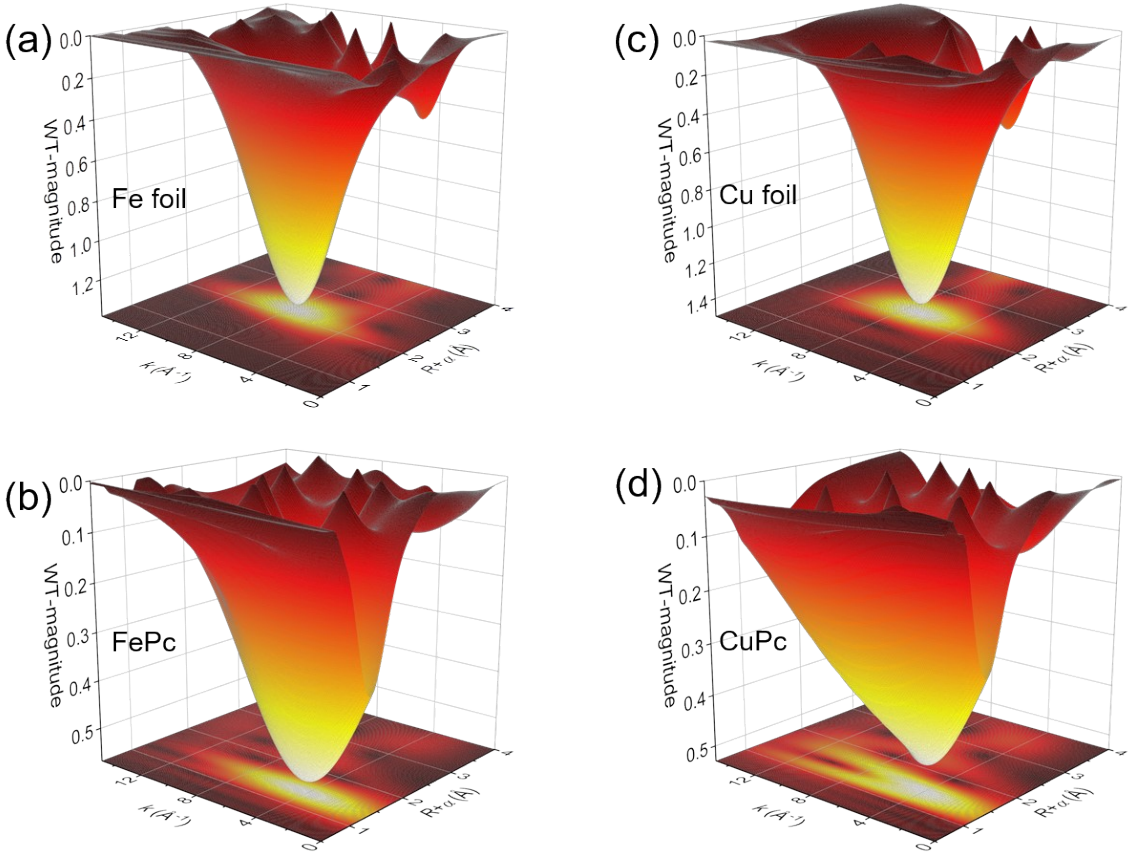

Figure S11. WT-EXAFS data of (a) Fe foil, (b) FePc, (c) Cu foil, and (d) CuPc at Fe K-edge or Cu K-edge.

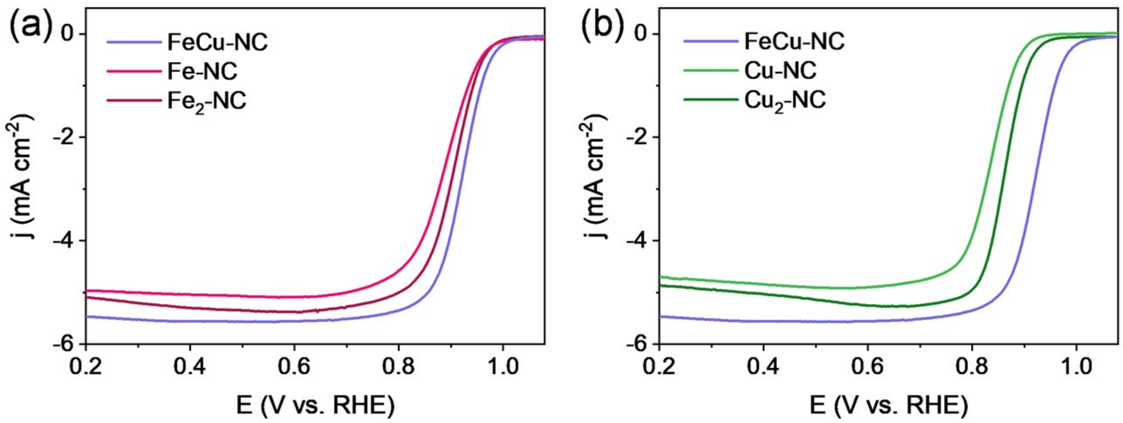

Figure S12. ORR polarization curves of the samples with different metal contents in O_2-saturated 0.1 M KOH solution with a rotation rate of 1600 rpm and a sweep rate of 10 mV s^{-1}.

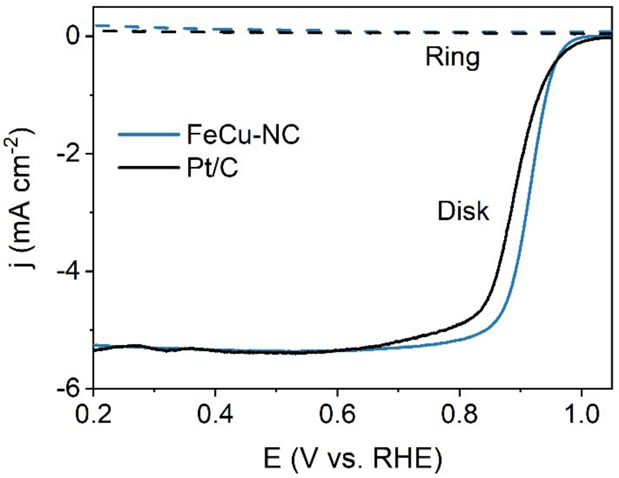

Figure S13. RRDE ORR polarization curves of FeCu-NC and Pt/C in O_2-saturated 0.1 M KOH solution with a rotation rate of 1600 rpm and a scan rate of 10 mV s^{-1}.

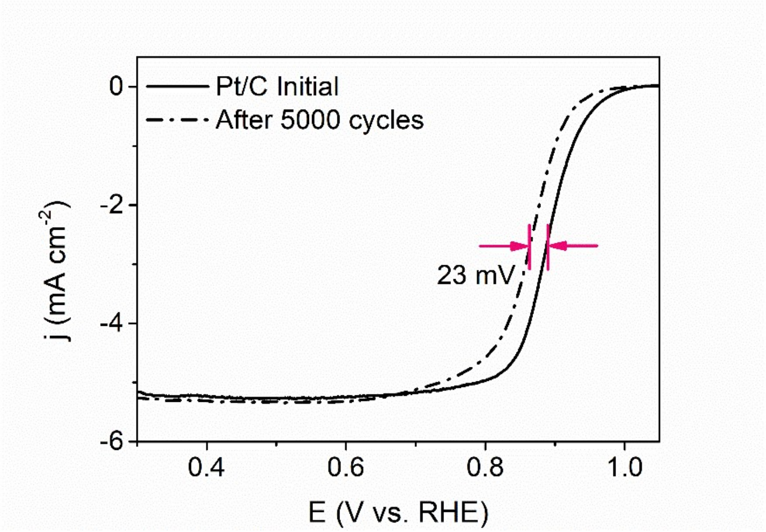

Figure S14. ORR polarization curves of commercial Pt/C in 0.1 M KOH solution with a rotation rate of 1600 rpm and a scan rate of 10 mV s^{-1} before and after the durability test.

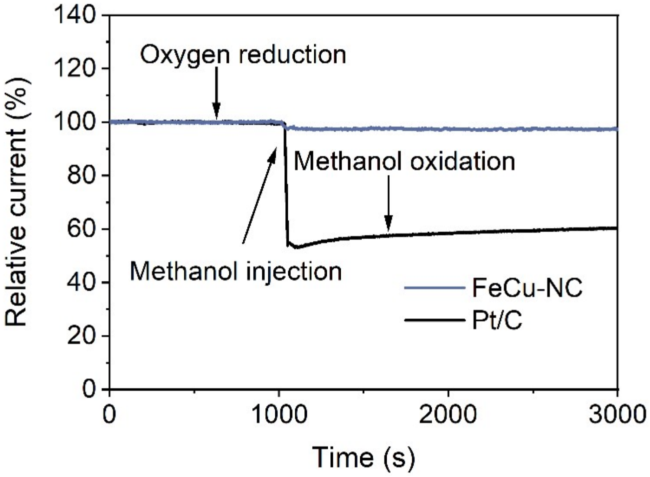

Figure S15. Methanol-crossover effect test of FeCu-NC and Pt/C.

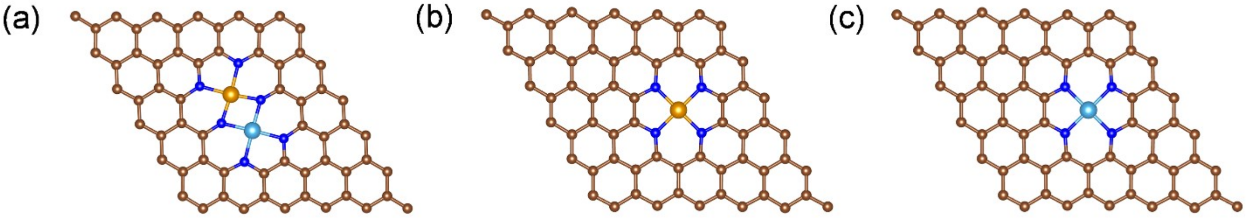

Figure S16. (a) FeCu-N_6, (b) Fe-N_4, and (c) Cu-N_4 as representative models for FeCu-NC, Fe-NC, and Cu-NC. The gray, cyan, orange, and blue spheres represented the C, N, Fe, and Cu atoms, respectively.

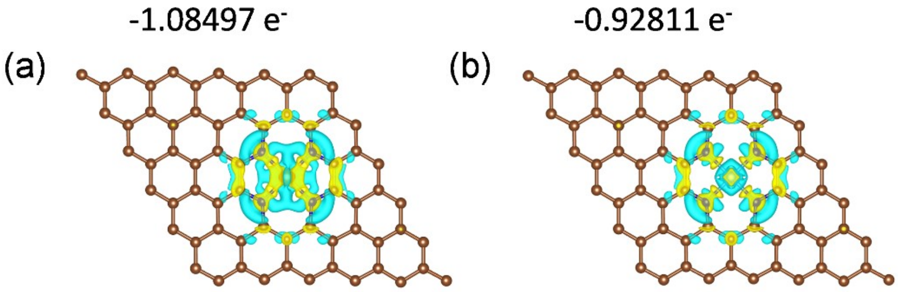

Figure S17. Bader charge analysis and charge density differences (the yellow area presented a charge density increase, and light blue area presented a charge density decrease) of (a) Fe-N_4 and (b) Cu-N_4.

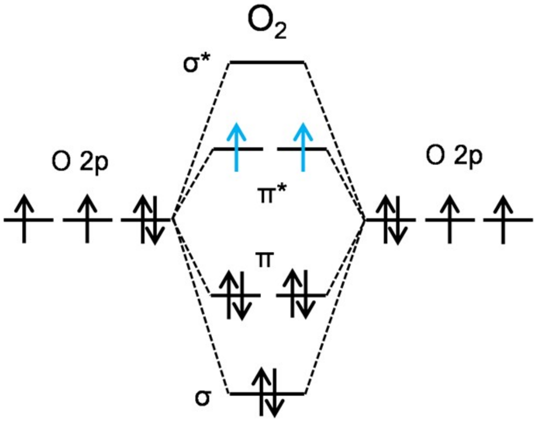

Figure S18. Molecular orbital diagram of O_2.

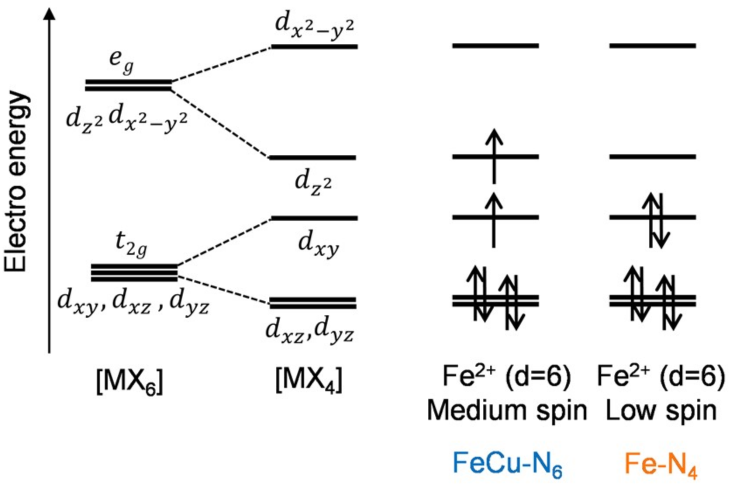

Figure S19. The d-electron configurations of Fe in FeCu-N_6 and Fe-N_4.

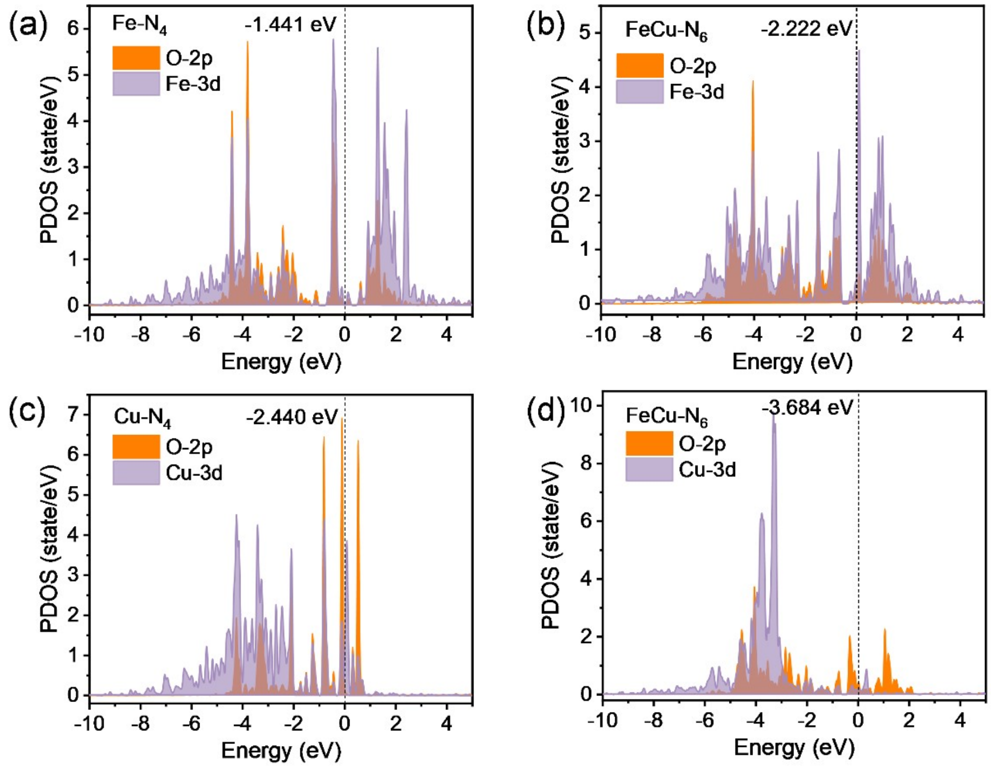

Figure S20. Projected density of states of metal sites and O sites after the adsorption of *O species.

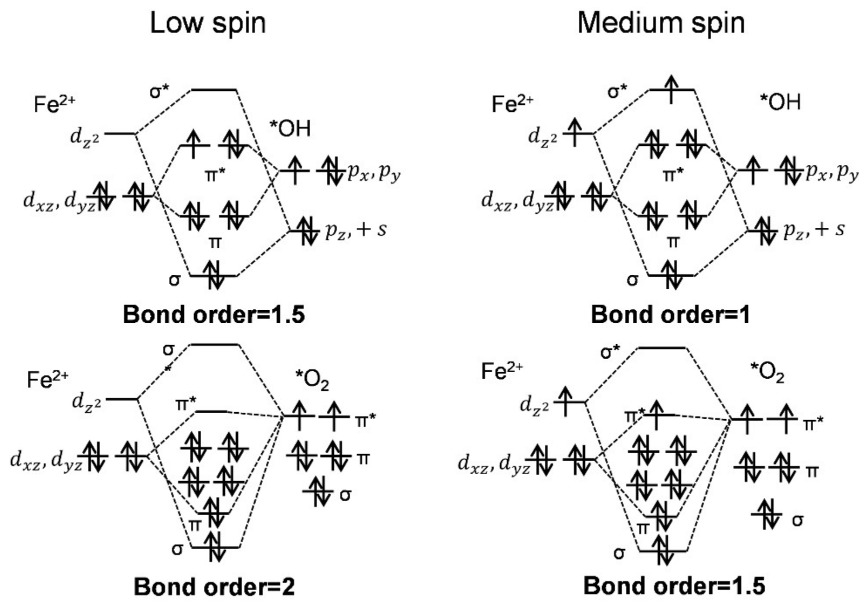

Figure S21. Diagrams of the orbital interactions between Fe in low and medium spin states and the oxygen-containing intermediates *OH and $*O_2$.

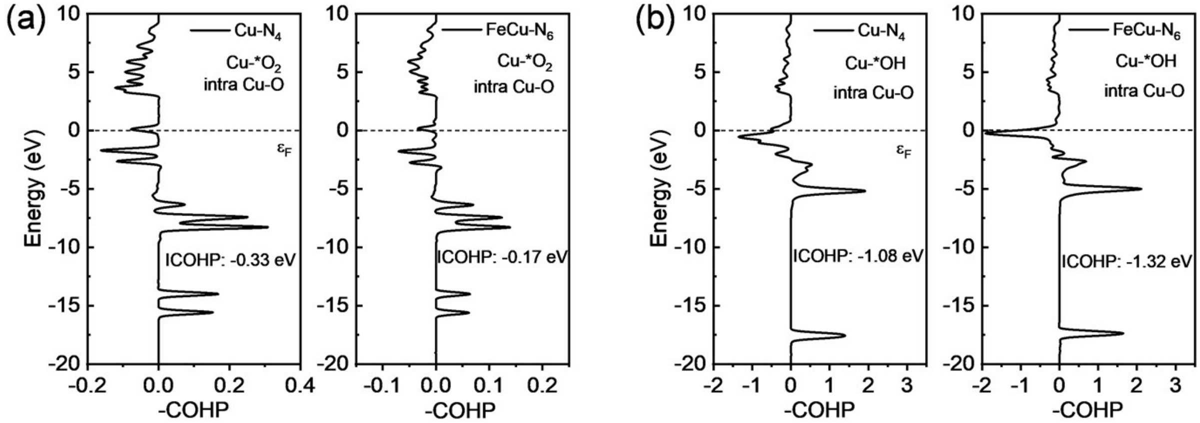

Figure S22. (a) pCOHP between the Cu active site center and O in the $*O_2$ adsorption. (b) pCOHP between the Fe active site center and O in the *OH adsorption.

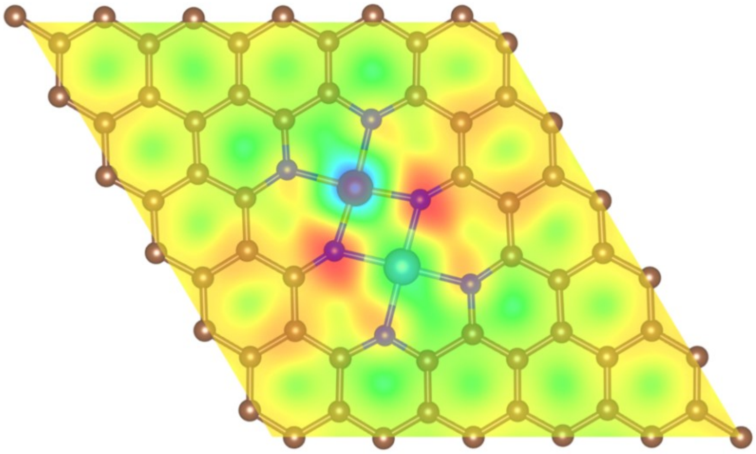

Figure S23. Electrostatic potential distribution diagram of FeCu-N6. The redder the area, the lower the electrostatic potential, while the bluer the place the higher the electrostatic potential, the more vulnerable to the attack of nucleophilic reagents (reaction intermediates).

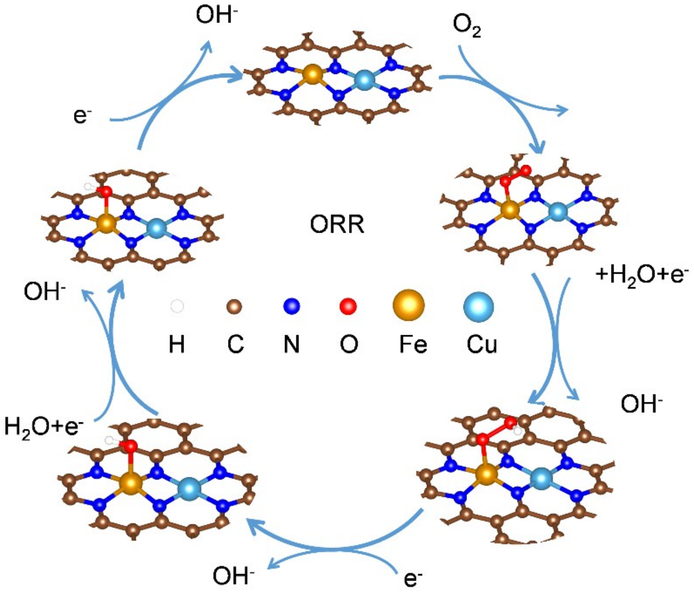

Figure S24. Schematic of ORR pathway.

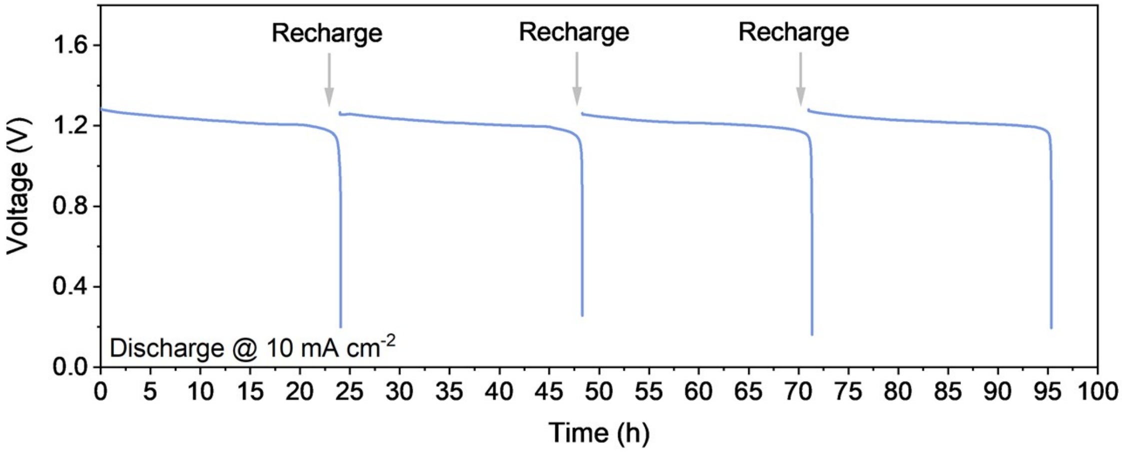

Figure S25. The long-time galvanostatic discharge curve of the zinc-air battery with FeCu-NC at 10 mA cm^{-2}, where the recharging is realized by changing the Zn anode.

3. Supporting Tables

Table S1. The content of different elements measured by XPS.

sample	C (at.%)	N (at.%)	O (at.%)	Fe (at.%)	Cu (at.%)
Fe-NC	83.71	4.16	11.53	0.61	-
FeCu-NC	81.84	5.19	11.92	0.59	0.46
Cu-NC	85.25	4.62	9.66	-	0.47

Table S2. Structural parameters extracted from the EXAFS fitting of FeCu-N-C. (S_0^2=1)

K-edge	Scattering pair	CN	R(Å)	$\sigma^2(10^{-3}Å^2)$	ΔE_0(eV)	R factor
Fe	Fe-N	3.48	1.94	6.61	-6.27	0.020
	Fe-Cu	0.87	2.44	6.61	-6.27	
Cu	Cu-N	4.38	1.98	14.8	-2.65	0.012
	Cu-Fe	1.09	2.43	14.8	-2.65	

S_0^2 is the amplitude reduction factor; CN is the coordination number; R is the interatomic distance (the bond length between central atoms and surrounding coordination atoms), σ^2 is Debye-Waller factor (a measure of thermal and static disorder in absorber-scatterer distances); ΔE_0 is edge-energy shift (the difference between the zero kinetic energy value of the sample and that of the theoretical model). R factor is used to value the goodness of the fitting.

Table S3. Comparison of ORR performance in 0.1 M KOH electrolyte between FeCu-NC with other non-precious metal catalysts reported recently.

Catalyst	Mass loading (mg cm^{-2})	Onset potential (V vs. RHE)	Half-wave potential (V vs. RHE)	Reference
FeCu-NC	0.5	1.03	0.918	This work
Fe-N_4SP	0.5	0.98	0.912	*Energy Environ. Sci.* **2024**,17, 249-259
Fe-Zn@SNC	0.51	0.99	0.86	*Angew. Chem. Int. Ed.* **2023**, 62, e202301833
Fe-N,O/G	0.204	1.0	0.86	*Energy Environ. Sci.* **2023**, 16, 2629-2636
Fe_H-N-C	0.6	1.0	0.91	*Adv. Mater.* **2023**, 35, 2210714
FeNC-V_N	0.3	0.99	0.902	*J. Am. Chem. Soc.* **2024**, 146, 7, 4803-4813
YN_4-Cl	0.41	0.93	0.85	*Adv. Mater.* **2023**, 35, 2300381
P-O/FeNC-SAC	N/A*	0.96	0.912	*ACS Energy Lett.* **2023**, 8, 11, 4531-4539
Fe_3Co_7-NC	0.3	1.05	0.893	*Adv. Funct. Mater.* **2023**, 33, 2212299
As-DC1-1050	0.56	1.016	0.901	*Energy Environ. Sci.* **2024**, 17, 123-133
Fe-N-C/Fe_3C-op	0.835	1.02	0.911	*Adv. Sci.* **2023**, 10, 2301656
Fe/I-N-CR	0.2	1.025	0.915	*Adv. Mater.* **2024**, 36, 2412978
Re-SAC	0.09	1.0	0.89	*Energy Environ. Sci.* **2024**, 17, 5892
cc-Fe	0.5	0.95	0.866	*Adv. Funct. Mater.* **2025**, 35, 2424401
SA-Fe-SNC@900	0.255	1.01	0.876	*Adv. Mater.* **2023**, 35, 2209948
SA-Fe^{III}/SNPC	0.6	0.99	0.91	*Adv. Funct. Mater.* **2023**, 33, 2304277
Mn_1@Fe-N-C/CNTs	0.416	1.01	0.89	*ACS Nano* **2024**, 18, 1, 750-760
CoN_4-Cr	N/A*	0.91	0.86	*Angew. Chem. Int. Ed.* **2024**, 63, e202400577
Fe_x/FeN_3S_1-C	0.255	1.01	0.9	*Energy Environ. Sci.* **2024**, 17, 4746-4757
FeCo-SAs	0.64	0.97	0.884	*ACS Nano* **2024**, 18, 20, 13006-13018
Fe_2/Ni-N-HCMs	0.5	1.04	0.88	*Angew. Chem. Int. Ed.* **2024**, 64, e202421168

*N/A indicates that the value was not provided in the original publication.

Table S4. The magnetic moment of different metal sites.

Metal sites	FeCu-N_6(Fe)	FeCu-N_6(Cu)	Fe-N_4	Cu-N_4
Spin moment (μB)	2.151	0.53	1.913	0.528

4. References

1. B. Zhao, J. Song, R. Ran and Z. Shao, *Int. J Hydrogen Energy*, 2012, **37**, 1133-1139.
2. B. Zhao, L. Sun, R. Ran and Z. Shao, *Solid State Ion.*, 2014, **262**, 313-318.
3. P. E. Blöchl, *Phys. Rev. B*, 1994, **50**, 17953.
4. G. Kresse and D. Joubert, *Phys. Rev. B*, 1999, **59**, 1758.
5. J. P. Perdew, K. Burke and M. Ernzerhof, *Phys. Rev. Lett.*, 1996, **77**, 3865.
6. G. Kresse and J. Hafner, *Phys. Rev. B*, 1993, **47**, 558.
7. G. Kresse and J. Furthmüller, *Phys. Rev. B*, 1996, **54**, 11169.
8. V. Wang, N. Xu, J.-C. Liu, G. Tang and W.-T. Geng, *Comput. Phys. Commun.*, 2021, **267**, 108033.
9. K. Momma and F. Izumi, *J. Appl. Crystallogr.*, 2011, **44**, 1272-1276.
10. J. K. Nørskov, J. Rossmeisl, A. Logadottir, L. Lindqvist, J. R. Kitchin, T. Bligaard and H. Jonsson, *J. Phys. Chem. B*, 2004, **108**, 17886-17892.
11. J. K. Nørskov, T. Bligaard, A. Logadottir, J. Kitchin, J. G. Chen, S. Pandelov and U. Stimming, *J. Electrochem. Soc.*, 2005, **152**, J23.